RESEARCH ARTICLE | OCTOBER 23 2023

Gaussian process regression for the side-by-side foil pair

Boai Sun (孙博爱) ; Ruipeng Li (李瑞鹏) ; Weicheng Cui (崔维成) ; Dixia Fan (范迪夏) ; Yihan Shen (沈意涵)

Physics of Fluids 35, 107133 (2023)
https://doi.org/10.1063/5.0172279

Physics of Fluids ARTICLE pubs.aip.org/aip/pof

Gaussian process regression for the side-by-side foil pair

Cite as: Phys. Fluids **35**, 107133 (2023); doi: 10.1063/5.0172279
Submitted: 14 August 2023 · Accepted: 2 October 2023 ·
Published Online: 23 October 2023

Boai Sun (孙博爱),[1,2] Ruipeng Li (李瑞鹏),[2,3,a)] Weicheng Cui (崔维成),[2,3] Dixia Fan (范迪夏),[2,3] and Yihan Shen (沈意涵)[4,5,a)]

AFFILIATIONS

[1]Zhejiang University-Westlake University Joint Training, Zhejiang University, Hangzhou 310027, China
[2]Key Laboratory of Coastal Environment and Resources of Zhejiang Province, School of Engineering, Westlake University, Hangzhou 310030, China
[3]Institute of Advanced Technology, Westlake Institute for Advanced Study, Hangzhou 310024, China
[4]Department of Second Dental Center, Shanghai Ninth People's Hospital, Shanghai Jiao Tong University School of Medicine, Shanghai 201999, China
[5]College of Stomatology, Shanghai Jiao Tong University, Shanghai 200011, China

[a)]**Authors to whom correspondence should be addressed:** liruipeng@westlake.edu.cn and shenyihandentist@163.com

ABSTRACT

The mutual interaction among multiple fish during schooling has significant implication on motion pattern control and hydrodynamic optimization. However, the collective motion of multiple objects in a flow field forms a vast parameter space, causing difficulty in comprehensively analyzing and considering each parameter. To address this issue, the problem is simplified to a foil pair oscillating in a side-by-side configuration in a two-dimensional flow. Moreover, the Gaussian process regression predictive algorithm is combined with the fast and robust boundary data immersion method CFD algorithm to form a iteration loop for value prediction of the large parameter space. Through a relatively small number of simulations (around 1000 data points), we obtained predictions for the entire four-dimensional parameter space that consists of more than 160 000 parameter sets, greatly improving the computational efficiency. After obtaining the predicted space, we analyzed the interactions between different parameters and specially described the mechanism that gives rise to the unique effect of phase difference on the efficiency of the overall system and individual foils.

I. INTRODUCTION

Schooling is a common phenomenon in fish creatures.[1–3] In addition to social advantages, such as scaring away predators or improving cruising accuracy,[4–7] cluster swimming is also considered to effectively reduce energy consumption or rather improve efficiency compared with swimming alone.[8–10] A better understanding of fish schooling can not only reveal the laws of nature but also provide inspiration for the formation design and motion control of bionic propulsion devices and various underwater vehicles.

Much effort has been made to study the fish cluster swimming, and many research works have been carried out through biological observations, model experiments, and numerical simulations. Breder[11] observed that the side-by-side spacing of fishes in a school is usually a little over twice the distance from the side of a fish to the outer edge of the trail of vortices, and the maintenance of the integrity of vortices is important to swimming efficiency. The diamond pattern is analyzed by Weihs,[1] in which water velocity relative to the vortices is induced by the vortex trail and utilized by the followers. In contrast, eels tend to swim in a synchronized fashion parallel to each other.[12] Similarly, when Hemigrammus bleheri, a popular aquarium fish, are forced to swim fast, the most frequent configuration is the phalanx formation with all individuals swimming side by side.[13] The study also discovers that displacement structures tend to have a closer side-by-side configuration at higher speeds through statistical observation.

Although the observation of real fish can reflect the swimming characteristics of the fish school, the formation is difficult to maintain and analyze quantitatively. To overcome the disadvantages, model experiments have been carried out correspondingly. In general, these works can be categorized into two cases. One case is implemented by robotic fish,[14–16] and the more adopted case is performed by characterized bionic hydrofoils for the sake of simplicity.[17–21] For instance, Godoy-Diana *et al.*[18] simulated side-by-side swimming fish by using

two rotating two-dimensional flexible plates to explore the effect of phase on the overall efficiency in parallel swimming. Dewey *et al.*[21] analyzed the flow field excited by the parallel flapping wake through the PIV method and quantified the different modes.

However, model experiments cannot completely simulate or reproduce the swimming process of real fish. They are also time-consuming and costly for different working conditions. With the fast development of powerful computing resources and efficient numerical algorithms, more and more studies are based on CFD approaches, both commercial software and open-source or in-house codes.[22–34] For instance, the swimming performance and vorticity structures of a mother-calf pair of fish in a two-dimensional flow field are studied by Tian *et al.*,[22] and it is found that the fish gain benefits by enhancing a reverse Karman street or diminishing a Karman street. The self-propelled locomotion of two, three, and four fish is studied by Dai *et al.*,[25] which suggests that passive hydrodynamic interactions can significantly mitigate the control challenges in schooling. Flow over traveling wavy foils in a side-by-side arrangement has been investigated by Dong and Lu[26] for in-phase and anti-phase traveling wavy movements. It is shown that lateral interference saves the swimming power in the in-phase case and enhances the forces in the anti-phase case. Considering that the evolution of the wake vortex in the actual flow field differs significantly from the two-dimensional case, Dong *et al.*[29] performed a three-dimensional hydrodynamic simulation of the parallel flexible flat plates. Liu *et al.*[31] then simultaneously integrated side-by-side and intermittent swimming to explore the comprehensive hydrodynamic effects on the fish group motion.

In spite of fruitful achievements mentioned above, the need remains for a comprehensive analysis method of multiple parameters that emerges in fish schooling studies. The number, size, formation, and movement mode of individuals in the fish school makes the analysis of cluster swimming a complicated problem with enormous parameters. In fact, even in the most simplified cases of aggregate motion, such as the two-fish/foil swimming study, multiple key parameters still form a substantial high-dimensional parameter space for experiment exploring. As brute force search of the whole space requires unacceptable computational consumption, the algorithm capable of high-speed hydrodynamic simulation is needed, along with the algorithm capable of predicting the output for high-dimensional parametric data space with the dataset obtained from limited experiments. In this study, the boundary data immersion method (BDIM) is used as the simulation platform, and Gaussian process regression (GPR) is conducted to predict and analyze the characterized parameter set and further explore the flow fields.

The rest of this paper is organized as follows: The methods and numerical models are presented and explained in Sec. II. The model result, the generated prediction space, and the characteristic flow fields are numerically evaluated and illustrated in Sec. III. Finally, concluding remarks are addressed in Sec. IV.

II. PHYSICAL MODEL AND NUMERICAL METHOD

A. Model description

This study is motivated to optimize the high-dimensional parameter space for a side-by-side foil pair. As shown in Fig. 1, two standard NACA0012 foils are fixed in a uniform two-dimensional flow field, and the bodies oscillate in a sinusoidal pattern around the mass centers. The two mass centers are in the same position in the x-direction,

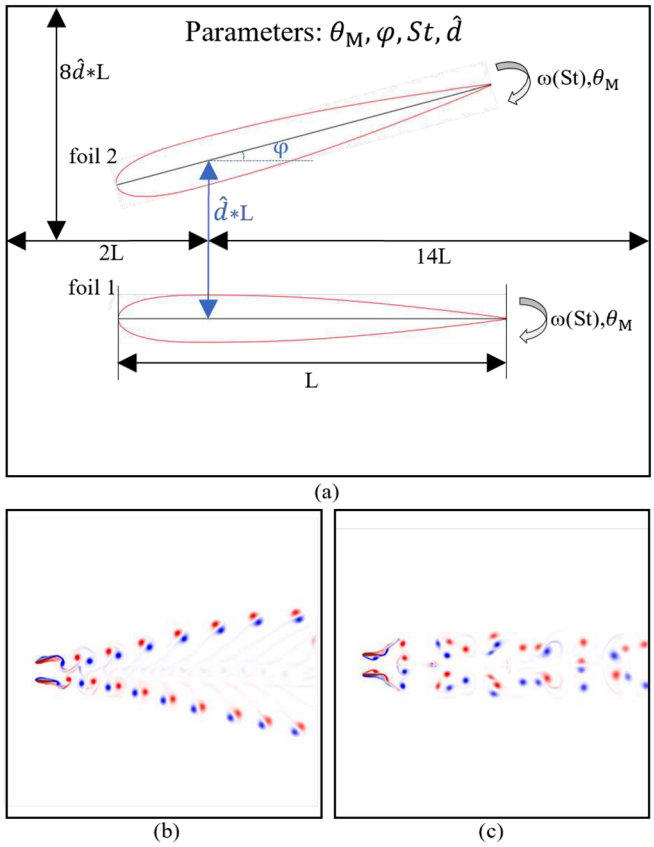

FIG. 1. (a) Definition sketch. To achieve esthetic appeal, we have adjusted the scale of the spatial relationships within the image accordingly. (b) and (c) Two simulation frames captured during the iteration process, presenting the actual scale of the simulation.

while the distance in the y-direction is an important parameter for the performance analysis.

The oscillating motions of the foils are characterized by four parameters. The general motion of the foils is defined by the swing amplitude of the foil θ_M and the Strouhal number St describing the frequency of the motion, which is defined as

$$St = \frac{\omega L}{2\pi U_\infty},$$

where ω is the frequency of the flapping motion, L is the chord length, and U_∞ is the inflow velocity from the left side. In this study, we select the foil chord as the characteristic length, for the distance swept by the foil tail is directly related to θ_M. For simplicity, the oscillating amplitude and frequency of two foils are set to be equal. Apart from these two parameters, we also define φ and $\hat{d}$, representing the phase difference and the distance of the mass centers in the y-direction between the two foils. In our study, the Reynolds number, defined as

$$Re = \frac{\rho U_\infty L}{\mu},$$

is set to 10 000, where ρ and μ represent the density and the dynamic viscosity coefficient of the fluid. The motions of the foil pair are numerically described as

$$\begin{cases} \theta_1(t) = \theta_M \sin(\omega t) \\ \theta_2(t) = \theta_M \sin(\omega t + \varphi), \end{cases} \tag{1}$$

where ω is related to the Strouhal number St defined above.

Three essential non-dimensional coefficients are calculated to describe the general and individual propulsion effect of the foil pair in the steady state, including the thrust coefficient C_T, the power consumption coefficient C_P, and the propulsion efficiency η. The thrust coefficient C_T is defined as

$$\begin{cases} C_T = \dfrac{\bar{F}_x}{1/2\rho U_\infty^2 L} \\ \bar{F}_x = \dfrac{1}{\tau}\displaystyle\int_0^\tau F_x(t)\mathrm{d}t, \end{cases} \tag{2}$$

where $\bar{F}_x$ stands for the mean force in the x-direction and τ for the accumulated time with a stable flow field in the simulation. Similarly, the power consumption coefficient C_P is defined as

$$\begin{cases} C_P = \dfrac{\bar{P}}{1/2\rho U_\infty^3 L} \\ \bar{P} = \dfrac{1}{\tau}\displaystyle\int_0^\tau M_\theta(t)\dfrac{\mathrm{d}\theta}{\mathrm{d}t}\,\mathrm{d}t, \end{cases} \tag{3}$$

where $\bar{P}$ stands for time-averaged power consumption and $M_\theta(t)$ for the pitching torque. Since the mass centers of the foil pair are fixed in this study, the power consumption only consists of foil rotation. Finally, we have

$$\eta = \frac{C_T}{C_P} \tag{4}$$

and define η as the overall propulsion efficiency. A fish-like propulsor's performance is mainly defined by thrust and efficiency, so C_T and η of the foil-pair and each foil are chosen as the simulation outputs.

Inheriting the above-mentioned definition, a four-dimensional parameter space composed of θ_M, φ, St, and $\hat{d}$ is formed for the analysis of the foil pair. The brute force search approach takes up considerable computational resources, increasing exponentially with the number of parameters. The method capable of conducting prediction in the overall parameter space by a smaller training set is needed. Therefore, a combined solution (BDIM + GPR) is proposed in this study. On the one hand, we apply a fast and highly robust BDIM for fast simulations. On the other hand, the GPR algorithm to predict the entire space is applied based on the existing simulation dataset, and the parameters for computation in the next iteration are obtained. We continuously expand the dataset and update the prediction until the relative error converges to the ideal situation. In the simulations, variation intervals for the four parameters are set as follows: $\theta_M \in [3°, 30°]$, $\varphi \in [0°, 180°]$, $St \in [0.3, 1.2]$, and $\hat{d} \in [0.8, 1.5]$.

B. Boundary data immersion method

The boundary data immersion method (BDIM)[35–37] is a novel treatment of general boundary conditions in fluid–solid coupled problems, combined with the advantages of robustness and accuracy. The BDIM establishes analytical meta-equations by superimposing the original multi-domain problem in a single domain with an immersed smooth interface. As the traditional compliant boundary method strictly separates the solid domain from the fluid domain, the mesh in the fluid domain is irregular and needs updating in each time step, which creates a substantial computational demand and makes it challenging to construct meshes at sharp points and objects with deformations. On the other hand, the classical immersed boundary method ensures a flat mesh, while the fluid motion is corrected at multi-phase boundaries (e.g., rigid body surfaces) using a field distribution in the form of bulk forces, which gives up the influence of higher-order terms in hydrodynamics and therefore loses accuracy.

Compared with the two existing mainstream approaches mentioned above, the BDIM blurs the boundaries of the different domains, combining the rigid body domain B, fluid domain F, and boundary layer S into the whole domain Ω. By implementing a finite smoothing width kernel on the boundary, the method enforces the boundary conditions of the solid object onto the fluid domain to ensure that the no-slip condition at the object's surface is satisfied. When employing this method for temporal iteration and solving the velocity and pressure matrices at the new time step, the equations utilized are as follows:

$$\vec{\nabla}\cdot\left(\frac{1-\delta_\varepsilon^B}{\rho^0}\vec{\nabla}p_\varepsilon^0\right) = \vec{\nabla}\cdot\left[\vec{r}_\varepsilon^0 + \frac{\vec{u}_\varepsilon^0}{\Delta t}\right], \tag{5}$$

$$\frac{\vec{u}_\varepsilon' - \vec{u}_\varepsilon^0}{\Delta t} = \vec{r}_\varepsilon^0 - \frac{1-\delta_\varepsilon^B}{\rho^0}\vec{\nabla}p_\varepsilon^0, \tag{6}$$

where the continuity function is fulfilled, and the first-order estimate of the new velocity and pressure field is calculated. More details can be referred to the full description in Weymouth and Yue.[36] The method also utilizes a special remapping technique to transfer the displacement information of the object's surface to the surrounding fluid domain, thereby updating the boundary conditions during object motion.[37]

Based on the above-mentioned method, Weymouth completed a program implementation of BDIM based on the Java language with the processing visualization platform. Since practically all meaningful computational intervals are within the boundary domain, the algorithm is very suitable for a single computational kernel in hydrodynamics, while the calculation retains high-order accuracy. More importantly, the BDIM algorithm is particularly ideal for objects in motion deformation due to the concise delineation of regions. It is worth noting that BDIM objectively overlaps different domains, which causes a part of the boundary structure distortion and a loss in shape accuracy, yet the method is still suitable for the modeling in this study. The validation of the algorithm and the mesh convergence tests are conducted as shown in Appendix A.

C. Gaussian process regression

The Gaussian process regression (GPR), a recently developed machine learning regression method with a rigorous statistical learning theoretical foundation, is well adapted to complex problems with high dimensionality, small samples, and nonlinearities with a strong generalization capability. Compared with neural networks and support vector machines, the GPR has the advantages of easy implementation,

adaptive acquisition of hyperparameters, flexible nonparametric inference, and probabilistic significance of output.

The GPR algorithm includes two steps. First, in the prediction process, from the function space perspective, a Gaussian process describes the function distribution, and Bayesian inference is performed directly in the function space. The Gaussian process is the set of any finite random variables with a joint Gaussian distribution, whose properties are determined by the mean and covariance functions. The primary equations for the joint prior distribution of observations y and predictions f_* are as follows:

$$\begin{bmatrix} y \\ f_* \end{bmatrix} \sim N\left(\left[0, \quad \begin{bmatrix} K(X,X)+\sigma_n^2 I_n & K(X,x^*) \\ K(x^*,X) & k(x^*,x^*) \end{bmatrix}\right]\right), \tag{7}$$

where K and k represent different covariance matrices between test point or training set. Second, in the training process, the algorithm chooses different covariance functions, such as squared exponential covariance. The negative log-likelihood function of the conditional probability of the training sample $L(\theta) = -\log p(y|X,\theta)$ is established, along with the bias against the hyperparameters θ. Then, the optimization methods are used to minimize the partial derivatives to obtain the optimal solution of the hyperparameter, by minimizing the $L(\theta)$ with the equation as follows:

$$\frac{\partial L(\theta)}{\partial \theta_i} = \frac{1}{2}\mathrm{tr}\left(\left(\alpha\alpha^T - C^{-1}\right)\frac{\partial C}{\partial \theta_i}\right), \tag{8}$$

with $C = K_n + \sigma_n^2 I_n$ and $\alpha = (K_n + \sigma_n^2 I_n)^{-1} y = C^{-1} y$. After obtaining the optimal hyperparameters, the predicted values and their variances corresponding to the test point can be calculated. Here, only a very brief introduction of GPR is presented, and more details can be referred to Rasmussen and Williams.[38]

In this study, we implement the GPR to collect the simulation results, re-predict the whole value space, and obtain the next parameter set with the highest uncertainty.

D. Iteration process

The main process of the coupled methods is illustrated in Fig. 2. In general, the overall iterative process consists of two parts. One is for the hydrodynamic algorithm, and the other is for the prediction part of the GPR algorithm. In detail, each iteration has four steps. First, the data model and the simulation environment are established according to the input parameters. To deal with the diverse parameter space, we design a dynamic flow field computational domain and a parametric auto-generated simulation process to couple with the GPR process. Second, once the CFD environment is set up, a fast hydrodynamic solution starts using the BDIM solver, and the outputs are obtained. Third, after adding the new data to the GPR model, the updated training set is used to re-predict the overall space and get the variation of the prediction space to analyze the data in multiple dimensions. Finally, the convergence of the iterations is evaluated by the relative error between two adjacent processes. Till the error converges, the parameter set for a new simulation round would be given according to the maximum variation point. When the average error is less than the threshold, the training is considered completed, and the final result is obtained. In the context of the obtained GPR prediction model, the

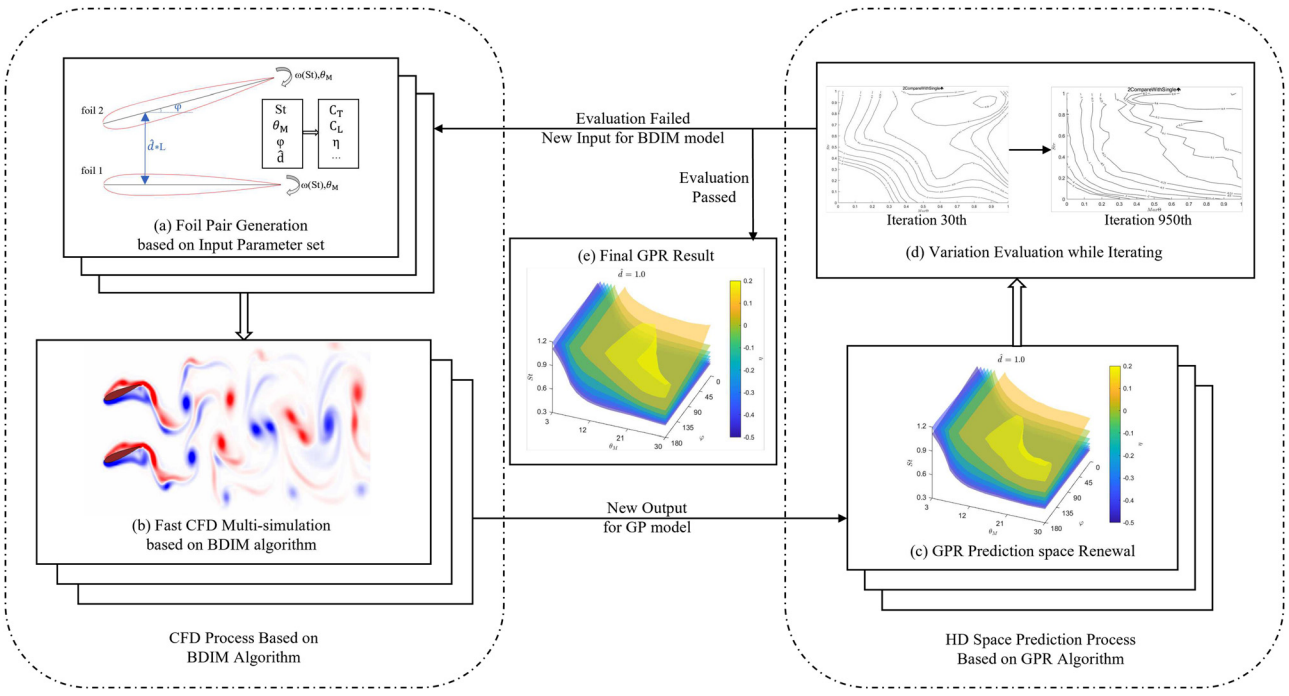

FIG. 2. The iteration process of the present study. The dashed box on the left represents the CFD algorithm procedure. After receiving the parameter set selected from the previous iteration, a solver is generated, and the corresponding result is calculated. The algorithm then passes the results to the GPR algorithm in the dashed box on the right, which uses all the existing data to predict, validate the parameter space, and select the parameter combination for the next iteration.

ALGORITHM 1: GPR for side-by-side flapping foils.

Input: flapping foil-pair parameters $\theta_M, \varphi, St, \hat{d}$
Output: output $C_{T1}, C_{T2}, C_{Tall}; \eta_1, \eta_2, \eta_{all}$

```
for iteration i do
    Obtain X_i = {θ_M, φ, St, d̂} from initialization or results of iteration i-1
    Generate new foil pairs and BDIM solver environment
    Obtain Y_i(C_t or η) in CFD solver
    Predict Y and VarY in whole parameter space based on all previous {X_1...X_i; Y_1...Y_i}
    Validation of prediction space
    if Validation passed then
        Prediction result output
        Iteration stop
    else
        Select new X_{i+1} with largest VarY for (i+1)th iteration
    end
end
```

results from CFD and GPR prediction are compared as shown in Appendix B, from which it can be observed that the predictions generated by the GPR model exhibit a high level of accuracy across the entire parameter space and effectively capture the variations in individual parameters.

III. RESULT AND DISCUSSION

A. Results of GPR process

The evolution of the relative error between two steps as iterations proceed is presented in Fig. 3. We compare the prediction space with the results of the previous cycle, and the output relative error as shown in Fig. 3 converges rapidly after hundreds of iterations. The subfigures alongside the main error plot represent the three-dimensional contour plots of efficiency, setting $\hat{d} = 1.0$. The efficiency value prediction spaces in different iterations are displayed to explore the effect of the foil pair arrangement on the overall efficiency. Each plot shows the results of different iteration steps, from 30, 100, 200, 400, 600 to 1000. As the efficiency (η) prediction in the parameter space proceeds, it can be observed that the isosurface of high efficiency ($\eta > 0.2$) folds up, which indicates that the best overall efficiency is located at appropriately large rather than maximal θ_M and St values.

B. Parameter set discussion

1. C_T prediction results

In the analysis of the four-dimensional parameter space prediction results of C_T and η, it is obvious that among the four input parameters, θ_M, φ, and St have complex coupling relationships, while the effect of $\hat{d}$ on the overall flow field of the foil pair is monotonic. That is to say, as the foils approach or rather $\hat{d}$ decreases, the effect of the parallel foil pair locomotion will be enhanced continuously. Due to the limitation of only three dimensions being presented in figures, we set $\hat{d} = 1.0$ when analyzing the flow field in detail and interpret the

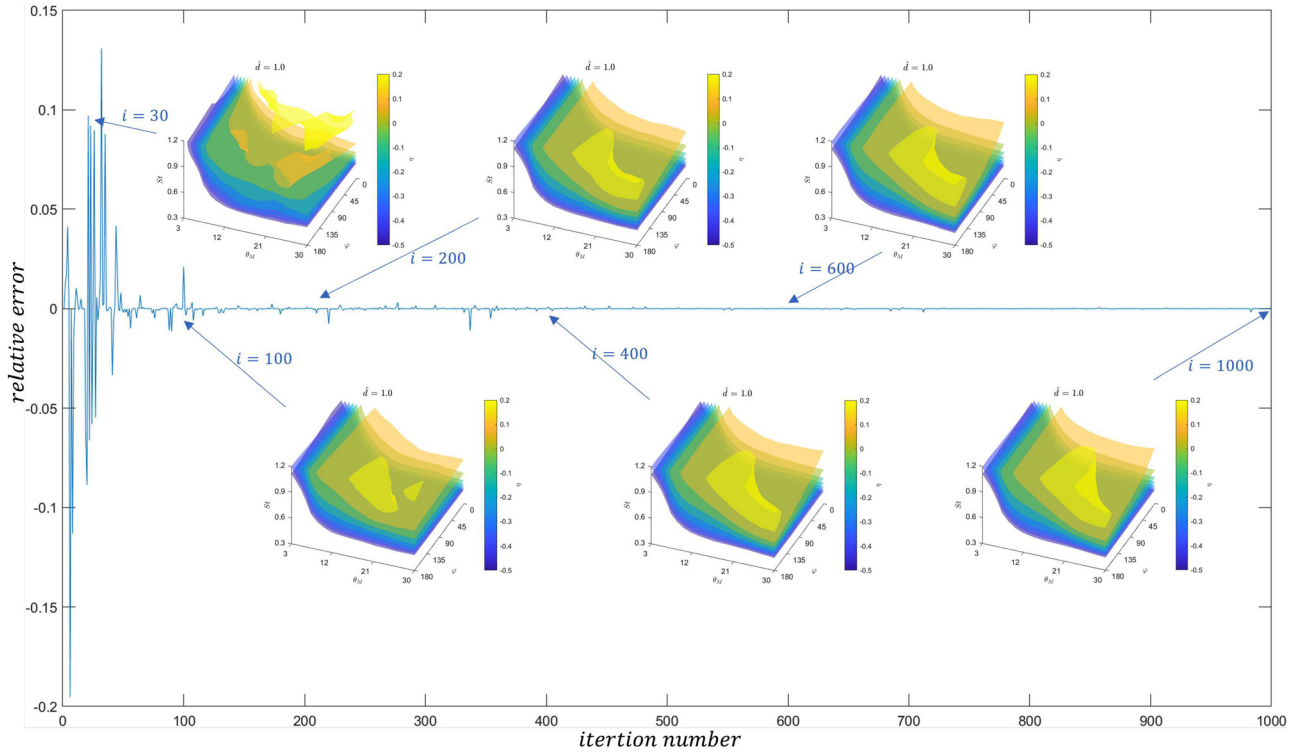

FIG. 3. The GPR prediction results evolve with the iterations. The results are plotted according to different iteration numbers 30, 100, 200, 400, 600, and 1000.

complex correlation between the remaining three parameters. In subplot (a) in Fig. 4, we also present the 3D distributions of C_T and η under the maximum and minimum distances. It can be seen that the effect and trend are consistent, while the numerical values are slightly different.

a. Overall analyze. The predicted values of the overall C_T parameter space are shown in subplot (a) in Fig. 4. Since $\hat{d}$ has monotonic effects on the performance of the foil pair, we focus on describing the other three parameters. In this example, we will analyze the case for $\hat{d} = 1.0$, and the predicted values at the maximum $\hat{d} = 1.5$ and minimum $\hat{d} = 0.8$ are also presented. Subplots (b)–(g) are discussions of interactions between every two parameters when the third one is fixed. Points with characteristic properties in these subfigures are selected to describe and analyze the flow field in subplots (b1)–(g2).

In subplots (b) and (c), we restrict the St of the motion to explore the effects of different amplitudes and phase differences on the motion. We select and present the 2D slices of the prediction space, respectively, representing the foil pair propulsion performance under small and large frequencies. In the case of low frequency (when $St < 0.3$), no matter how θ_M and φ are taken, the foil pair shows negative thrust in the flow field, which means the foils cannot move forward in the flow field by swinging. Such negative thrust generally increases with the amplitude θ_M and phase difference φ increasing, but the influence of θ_M accounts for the main factor. It can be interpreted that when the oscillating frequency is minor, the flow field is close to a static mode, and the low Strouhal number swing is difficult to generate the reverse Karman vortex at the tail. At the same time, the larger inclination angle will increase the incident flow area and then increase the resistance of the foil pair in the fluid. When the motion frequency is of medium size, as shown in subplot (b), the thrust generated by the swing is already evident. When θ_M and φ are given larger values, the optimal C_T can be obtained, and it is notable of the negative C_T region ($C_T < -0.06$) located in the middle right of the subfigure. When the swing angle θ_M is small, although the thrust generated by the swing is weak, the overall negative thrust is also insignificant due to the small incident area; when θ_M is large, the thrust generated by the swing is close to or exceeds the resistance from the incoming flow. However, with middle θ_M, the foils fail to produce appreciable hydrodynamic propulsion while receiving larger drag from the incident flow compared to the small θ_M case, forming a negative circular area in the predicted space. When the flapping frequency is large, the foil pair generates thrust on almost the whole space as long as the swing angle is not too small as shown in subplot (c). In addition, the overall thrust of the foil pair increases with the phase difference increasing to 180°. The mechanism of the influence caused by phase difference will be explained in detail in the next subsection.

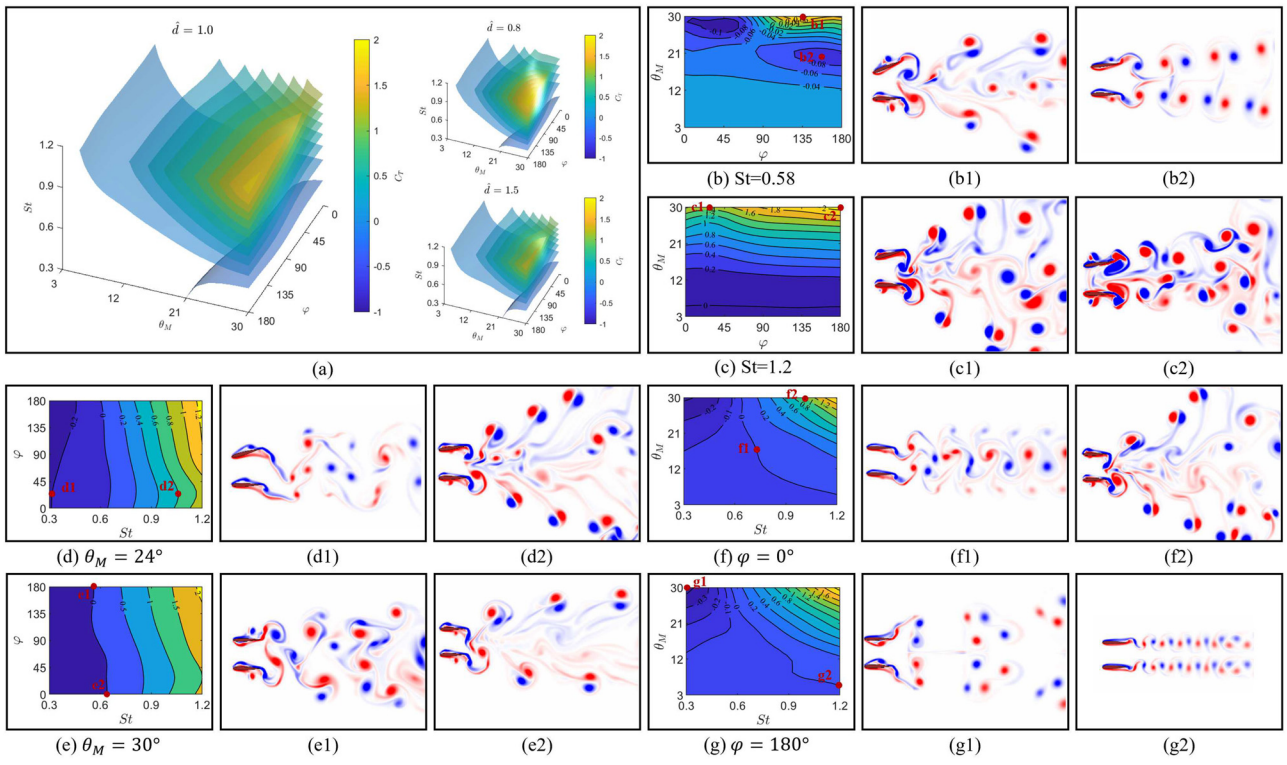

FIG. 4. C_T prediction results. (a) 3D distribution of the C_T prediction at $\hat{d} = \{1.0, 0.8, 1.5\}$. (b)–(g) Fix one parameter in θ_M, St, and φ and plot the relationship between C_T with the other two parameters, (b) and (c) for $St = 0.58, 1.2$, (d) and (e) for $\theta_M = 24°, 30°$, and (f) and (g) for $\varphi = 0°, 180°$. (b1)–(g2) The characteristic parameter combinations in (b–g) are selected to reproduce and analyze corresponding flow fields. The flow fields are selected for yielding max/min C_T, presenting a significant contrast between two selections, or the generated flow field with representative characteristics.

In subplots (d) and (e), we restrict the swing amplitude θ_M to explore the effects of St and φ on the thrust coefficient C_T. In general, the propulsion ability is positively correlated with St regardless of small or large amplitudes. However, in the case of small amplitudes, all combinations of frequencies and phases cannot generate overall positive thrust; in the case of large amplitudes, positive thrust can be generated when St is above 0.3. At the same time, it can be seen from subplot (d) that when St is small, φ is positively correlated with the negative thrust. While at large St numbers, φ is correlated with the positive thrust. It can be found that the increase in phase difference plays a role in strengthening the overall propulsion or resistance.

In subplots (f) and (g), we restrict the phase difference φ of the foil pair to explore the effects of St and θ_M on C_T. It can be observed that the distributions in different φ are all λ-shaped. In other words, C_T generated by the middle St and small θ_M is close to zero, representing the lower region in subplots (f) and (g); the combination of a large amplitude value and small frequency has a large negative thrust, and the combination of a large amplitude value and large frequency has a large positive thrust, which is consistent with our previous analysis.

b. Characteristic flow field analysis. Subplot (b1) shows the flow field of the motion with $\theta_M = 30^\circ$ and $St = 0.58$. As shown in subplot (b), most parameter combinations cannot generate positive thrust with small frequencies. However, under the condition of large amplitude and phase difference ($\theta_M = 30^\circ, \varphi = 140^\circ$), the maximum simulated total efficiency reaches 0.08, which is consistent with the GPR prediction value (point b1) as shown in subplot (b). Due to the phase lead of the upper foil 2, its thrust coefficient reaches 0.12 from numerical simulations, which is much higher than that of the lower foil 1 with a value of 0.06. The foil with phase lead will get better propulsion performance and efficiency, which is universal in the whole parameter space. The flow field of $\theta_M = 20^\circ$ and $\varphi = 160^\circ$ is shown in subplot (b2), where the lowest thrust coefficient appears. In general, as the swing amplitude θ_M continues to decrease, the resistance becomes smaller with the decrease in the inflow area. On the other hand, when the swing amplitude is set as a larger number, the propulsion ability of the foils is improved.

Subplots (c1) and (c2) describe the flow field for the maximum $\theta_M = 30^\circ$ and $St = 1.2$, whose generated thrust coefficients belong to the high propulsion range. In subplot (c1), φ is small, and the flow field is more dispersed. While in subplot (c2) for $\varphi = 180^\circ$, the flow field is more concentrated. The numerical simulation outputs are also consistent with the predicted values; the former simulated C_T value is 1.46, and the latter is 1.8 with a considerable advantage.

Subplots (d1) and (d2) demonstrate the influence of St on the flow field with $\theta_M = 24^\circ$ and a small phase difference. When the frequency of the foil flapping is small, the flow field at the trailing edge of the foils merges at the far end, resulting in a structure similar to a Karman vortex street. In subplot (d2), due to the higher frequency, distinct vortex shedding occurs on both sides of the flow field, but the flow field near the proximal end of the foil is turbulent and lacks the jet-like structure as shown in subplot (g1) in Fig. 5 for $\varphi = 180^\circ$.

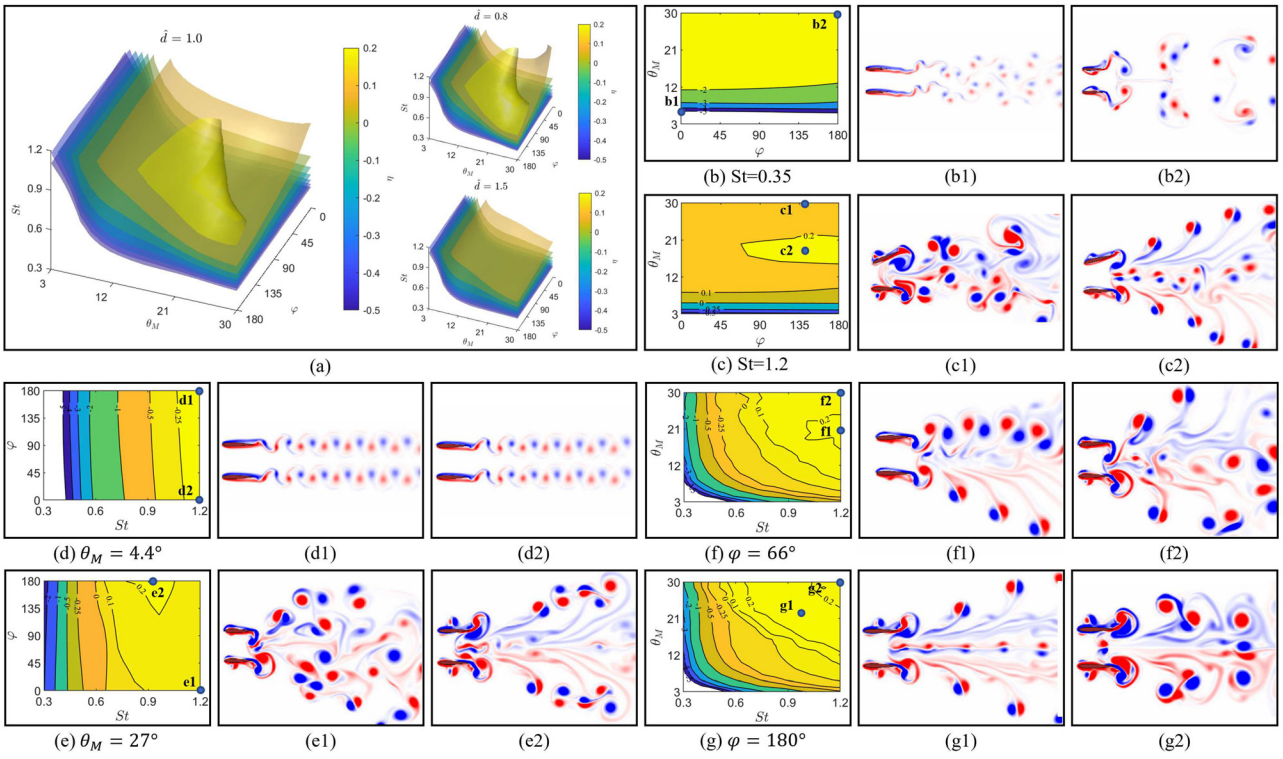

FIG. 5. Prediction results of efficiency (η). (a) 3D distribution of the η prediction at different $\hat{d} = \{1.0, 0.8, 1.5\}$. (b)–(g) Fix one of the three parameters apart from $\hat{d}$ and plot the relationship between η with the other two parameters, (b) and (c) for $St = 0.35$, 1.2, (d) and (e) for $\theta_M = 4.4^\circ$, 27°, and (f) and (g) for $\varphi = 66^\circ$, 180°. (b1)–(g2) The characteristic parameter combinations in (b)–(g) are selected to reproduce and analyze their flow fields.

Subplots (e1) and (e2) describe simulations with the largest swing amplitude $\theta_M = 30°$, while the thrust coefficients are both close to zero. Due to the large parametric space, there is a slight error in the C_T prediction of the zero value with the actual coefficients being 0.015 and 0.059 from the numerical simulation. In subplot (e1), because of the lower frequency, the foil pair with $\varphi = 180°$ does not form a stable jet-like structure, and the flow field even loses its symmetry. The reverse Karman vortex structure can be observed in subplot (e2), while the frequency required to obtain a positive thrust is higher than that of $\varphi = 180°$.

Subplot (f1) is for $\theta_M = 17°$, $\varphi = 0°$, and $St = 0.7$. The overall C_T is 8.4×10^{-4}, implying the thrust and drag achieve a relatively good balance. In this case, both the amplitude and frequency are moderate, and the phase difference is zero. The flow field of the foils is highly coupled, and an overall stable vortex structure is generated at the far end. In subplot (f2), θ_M and St are relatively large, and $\varphi = 0°$, resulting in a C_T value of 0.9, which is much smaller than that under the same other parameter settings with $\varphi = 180°$, as shown in subplot (g). From subplot (f2), it can be observed that the generated flow field is more divergent, and the structure in the middle is more chaotic, resulting in energy loss.

For the maximum phase difference $\varphi = 180°$, two extreme parameter combinations are selected to present, including subplot (g1) for the minimum St and maximum θ_M, and subplot (g2) for the maximum St and a very small θ_M. The largest negative thrust coefficient is produced by the parameter combination in case (g1). In the vorticity field, as the foils slowly swing, the Karman vortex street is generated due to the blocking of the incoming flow at the foil tail. With St at the minimum value of 0.3, the swing motion is slow and can be considered quasi-static, and the foils generate significant resistance with small power consumed. When θ_M is small at 5° and St is at its maximum in subplot (g2), the flow field of the foils does not merge due to the small swing amplitude. In this case, the thrust coefficient is 0.002, indicating that the propulsive effect of flapping roughly surpasses the incoming flow resistance.

2. Efficiency(η) prediction results

As shown in the predicted thrust coefficient space in Fig. 4, the relatively greater C_T values are generated with larger parameters, and the maximum thrust is also generated from the parameter set with all values at upper limits of θ_M, St, and φ. However, it is very different for the propulsion efficiency, which can be observed in subplot (a) in Fig. 5. With frequency and amplitude increasing, the energy consumed by the locomotion also enlarges. When St or θ_M exceeds a certain value, the propulsion efficiency starts to decrease. In fact, the two factors need to match in the appropriate value range so that maximum propulsion efficiency(η) can be achieved. Nevertheless, the proper combination of θ_M and St is also affected by φ between the foils. The latter will also significantly affect the efficiency of each and the overall efficiency.

a. Overall analyze. In subplots (b) and (c), different St are selected to investigate the effects of amplitude θ_M and phase difference φ on the foil pair efficiency. As shown in subplot (b) for $St = 0.35$, the propulsion efficiency η is negative in the entire parameter space. This is similar to the distribution of the thrust coefficient, where the negative thrust is generated due to the small flapping frequency. It is observed that the propulsion efficiency η increases with θ_M increasing (although still negative), which can be interpreted as an increase in thrust. However, the negative propulsion efficiency decreases (with an increase in the absolute value) as the phase difference increases. Note that in subplot (d) in Fig. 4, the negative thrust increases with φ increasing; it can be inferred that energy consumption also decreases as the phase difference increases. Although negative η is caused by the negative C_T and is not physically meaningful, we can still confirm that increasing phase difference can enhance thrust or drag and save energy. When St is at the maximum as shown in subplot (c), positive C_T and η are produced except for the amplitude of less than 4°. The propulsion efficiency η reaches 0.23 around $\theta_M = 20°$.

In subplots (d) and (e), two different flapping amplitudes are set to investigate the effects of frequency represented by St and phase difference φ on the efficiency of the foil pair. Under the small flapping amplitude $\theta_M = 4.4°$, the propulsion efficiency η is negative throughout the parameter space, indicating the inability to generate positive thrust. Under the large flapping amplitude $\theta_M = 27°$, the propulsion efficiency η reaches its maximum value near $St = 0.93$, and the value increases with the phase difference increasing. This also indicates that high efficiency in the foil pair requires an appropriate amplitude and frequency combination, while a larger phase difference generally benefits the overall efficiency.

In subplots (f) and (g), the phase difference is fixed to investigate the effects of St and θ_M on η. When the phase difference is small, the propulsion efficiency η increases monotonically with St increasing in the parameter range. The maximum propulsion efficiency η is produced when θ_M is around 20°. With all parameter sets with a very small phase difference φ, the propulsion efficiency η never reaches the high efficiency value of 0.2. In contrast, high efficiency is available at the large phase difference as shown in subplot (g) with $\varphi = 180°$ and a proper combination of θ_M and St. As shown in the upper right corner where θ_M and St take maximum values, the efficiency is not the largest. The effect of amplitude and frequency is not monotonous, while the highest propulsion efficiency η in the entire parameter space can be achieved at an appropriate parameter combination.

b. Characteristic flow field analysis. Subplot (b1) shows the flow field of the parameter combination with $\theta_M = 5°$, $\varphi = 0°$, and $St = 0.35$. Due to the small values of θ_M and St, and zero phase difference, the flow field of the foil pair slowly develops and merges in the far field. However, in the near field, a Karman vortex street is visible. The propulsion efficiency η for this simulation is -5.6 due to the very slight locomotion and low energy consumption, while the head of the foil overcomes large resistance, resulting in a large negative efficiency. In subplot (b2), keeping $St = 0.35$, set the phase difference $\varphi = 180°$ and $\theta_M = 30°$. The flow field exhibits symmetry forms due to the opposite phase of the flapping. Due to the large amplitude angle and low frequency, a significant interval between each swing leads to a shedding vortex in the flow field at the back. As shown in subplot (b1), the Karman vortex structure can be seen in the wake, which is consistent with the conclusion of a negative thrust.

In subplots (c1) and (c2), the phase difference φ is around 135° and $St = 1.2$. The propulsion efficiency for $\theta_M = 18°$ is higher than that for $\theta_M = 30°$. In subplot (c1), a stable flow field after the foil tails is failed to form due to the violent motion, while a reverse Karman

vortex structure is still visible in the vortex field. In contrast, subplot (c2) presents a clear and regular arrangement of the reverse Karman vortex street in the flow field, and a clear jet structure is also visible in the middle. It is worth noting that due to the phase difference, the upper foil with a leading phase obtains a higher efficiency in case (c1) and case (c2). The efficiency of the upper foil in case (c2) reaches 0.23, which is greater than the maximum foil-pair average efficiency value in the whole parameter space.

Subplots (d1) and (d2) represent the flow fields generated by a small amplitude and a high flapping frequency combined with different phase differences. In both simulations, Karman vortex streets appear after the foil, and the efficiency is less than zero. Due to the minimal flapping amplitude, the flow fields are relatively independent, and the efficiency is still slightly higher with the maximum phase difference, comparing the simulated result of cases (d1) and (d2).

In subplots (e1) and (e2), both the amplitude and frequency are large, and the phase difference is 0° and 180°, respectively. It can be seen that the flow field in subplot (e1) is relatively chaotic. However, clear reverse Karman vortex streets appear on both sides in subplot (e2), and a jet structure exists in the middle. In fact, the propulsion efficiency of the latter case with $St = 0.93$ is 22.0%, while $\eta = 16.5\%$ for the former case (e1).

Subplots (f1) and (f2) represent the flow field for $\varphi = 66°$ and $St = 1.2$. The overall efficiency of $\theta_M = 30°$ is lower than that of $\theta_M = 19°$. In the flow field generated by the case (f1), it can be observed that the flow fields of the two foils are coupled to each other, and the tail of the lower foil leads to a more intensive vortex structure, while the vortex behind the upper foil is relatively sparse. Correspondingly, in this case, as the overall simulated efficiency obtains a high value of 18%, the efficiency of the upper foil in the leading phase reaches 21%. In comparison, the efficiency of the lower foil is only 16%, indicating that the phase difference significantly impacts both the overall and individual foils.

Subplots (g1) and (g2) correspond to the flow field for the combination of large amplitude, frequency, and phase difference. When the amplitude and frequency are both set to the maximum value, a clear reverse Karman vortex street appears in the flow field, but the flow field at the rear is relatively chaotic. When $\theta_M = 22°$ and $St = 0.98$, the propulsion efficiency is up to 21%. It can be observed that the flow fields on both upper and lower parts are highly symmetrical, with regular reverse Karman vortex streets appearing on both sides and a clear jet structure in the middle, as shown in subplot (g1).

C. Flow analysis based on the whole parametric space

The previous analysis found that the foil with a leading phase always has a higher overall efficiency than the foil with a lagging phase whatever other parameters take, and the phase difference shows a unique influence in the general flow field. Within the same set of other parameters, the overall efficiency of the foil pair generally increases with the phase difference from 0° to 180°. An obvious competitive pattern occurs when the phase difference is around 90°, where the efficiency of one foil may be significantly reduced. In contrast, the other foil obtains much higher efficiency than the foil flapping alone. To analyze this phenomenon more quantitatively, three characteristic phase differences are selected according to the physical field of the foil pair under specific combinations of frequency, amplitude, and distance parameters.

The locomotion of the foil pair with no phase difference is illustrated in Fig. 6. The subplots (a)–(d) show the flow field vorticity at $t = 0,\ T/4,\ T/2,\ 3T/4$ in one period. The second four images present the corresponding pressure field. At $t = 0$, the foils are in the equilibrium position and swing upward together, and it is obvious that the pressure on the upper sides is greater, as shown in subplot (e). It should be noted that because the lower side of the upper foil is close to the upper side of the lower foil, the absolute pressure values on the inner sides are both smaller than the ones outside correspondingly.

At $t = T/2$, the pressure distribution is roughly the opposite of that of $t = 0$. At $t = T/4$, the foil tail is tilted upward. The upper surface of upper foil 2 is subjected to negative pressure, while the lower surface is subjected to positive pressure. Thus, the foil as a whole is subjected to a positive propulsion force. Also, it can be observed that the lower foil 1 receives a larger thrust during the swing upward, for having a larger positive pressure on the lower side and a smaller negative pressure on the upper side. At $t = 3T/4$, the pressure distribution is roughly similar but opposite to the above.

The locomotion of the foil pair in terms of the angular displacement is depicted in subplot (i), from which it is observed that the foils flap in the same sinusoidal pattern and there is no phase difference. Subplot (j) describes the thrust generated by the two foils, with the leftward propulsion regarded as positive. The red line represents the lower foil 1 data, the blue line represents the upper foil 2 data, and the yellow line represents the data of single foil locomotion with the same θ_M and St. It can be seen that the overall thrust generated by the foil pair is positive after integrating over time, indicating that the foils receive forward thrust through flapping locomotion in the incoming flow during the entire period. At the same time, during the motion process, the foil on the upward side of the flow direction (referring to upper foil 2 at around $t = T/4$ and lower foil 1 at around $t = 3T/4$) will later reach the maximum thrust value, but the peak value will be larger. Subplot (k) describes the power consumed by the foils. Compared with subplot (j), the different times of reaching peak value show that the moment of maximum thrust generation and the moment of rapid energy consumption do not actually coincide. When the foils oscillate to the balanced position, the rotational speed and resistance of both foils also reach the peak, and therefore, the power consumed is also at the maximum. It can be noted that the lower foil 1 at around $t = 0$ and upper foil 2 at around $t = T/2$ are subjected to greater resistance due to the larger negative pressure on the opposite side from the rotation direction, and therefore consumed more power, which can also be confirmed in subplots (e), (g), and (k). The mean velocity field is shown in subplot (l). It can be observed that the mean flow velocity in the x-direction behind the upper and lower foils is roughly the same near the tips, and an accelerating zone extending to the far field is shown on both sides. In contrast, the region between the accelerating zones has a smaller flow velocity distribution, and a reverse flow region emerges between the trailing edges of the foils.

Figure 7 corresponds to the locomotion of the foil pair with $\varphi = 180°$. The first four images describe the vorticity field at $t = 0,\ T/4,\ T/2,\ 3T/4$ in one period. The flow field exhibits strong symmetry, with the vortices on both sides gradually diverging outward, while a jet-like flow structure is formed in the middle. The pressure fields on the foil pair are shown in the middle four images. The foils are closing to each other in the equilibrium position at $t = 0$, and it is noted that the pressure on the inner sides is high. In comparison, a clear negative

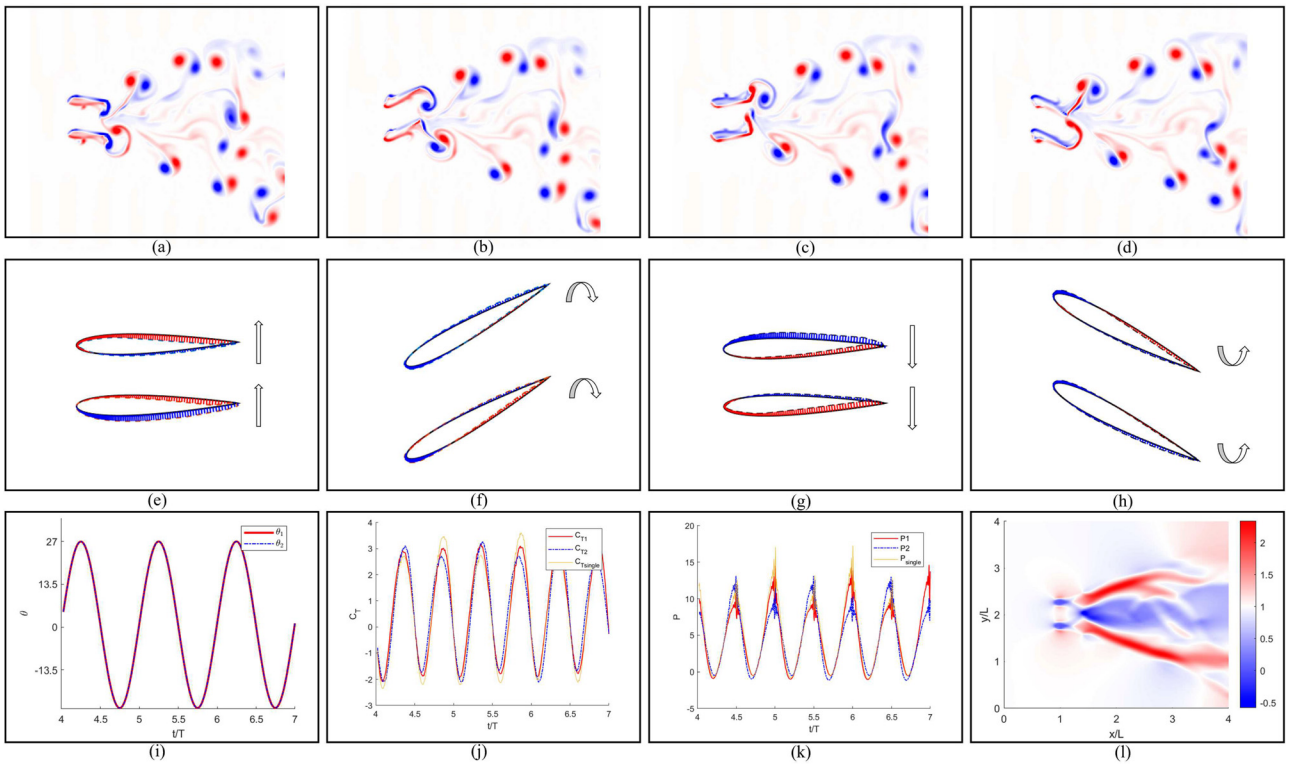

FIG. 6. The multi-physics field analysis of the foil pair when $\varphi = 0°$, and the other parameters are set as $\theta_M = 27°$, $St = 1$, and $\hat{d} = 1$. (a)–(d) Vorticity field at $t = 0$, $T/4$, $T/2$, $3T/4$ during a complete motion period. (e)–(h) Pressure distribution on the surface of the foil pair at the corresponding time. (i)–(l) Analysis of flow field data over multiple cycles, where (i) shows the phase of the two foils over three cycles, (j) and (k) shows the change of C_T and energy consumption P over time, and (l) shows the average of the velocity field in the x-direction over three complete cycles, indicating the tail flow velocity at the rear of the two foils. The yellow lines in (j) and (k) represent the single foil reference with the same motion parameters of θ_M and St.

pressure can be observed on the inner sides at $t = T/2$. As shown in subplot (g), where the foil tails are spreading out, the pressure on the outer sides of the two foils is positive, but the values are far less than those on the inner sides at $t = 0$. When the two foil tails are getting close, such pressure distributions produce thrust due to the transverse component along the inflow direction. At $t = T/4$ and $t = 3T/4$, the foils are inclined, and the downward foil surfaces are all subjected to positive pressure, and positive propulsion is generated.

Subplot (i) shows two foils flap in a sinusoidal pattern with an opposite phase. The thrust is presented in subplot (j), from which it is observed that C_T of each foil exhibits highly consistent. Compared with $\varphi = 0°$ or 90° cases, the overall thrust of the 180° system is also more significant, as shown in subplots (j) in Figs. 6–8. Additionally, during the flapping locomotion, there are two peaks in every period as shown in subplot (j). The higher peak happens when the foils are approaching in the last quarter of the period, which is consistent with the previous pressure analysis. Similar to the thrust coefficient C_T, the power consumption of each foil is the same in the whole period and has two different peaks as shown in subplot (k). When the foils swing to the equilibrium position, although the rotational speed is the same, the greater pressure difference as they approach leads to a greater force of resistance, consuming more energy while generating greater thrust. Subplot (l) shows the mean velocity field, which is symmetrical at the posterior with an accelerating region extending outward. The regions are less divergent and have a higher intensity than other cases, with a more significant reverse flow region between the two tail flows, compared with subplot (l) in Fig. 6.

Such perfectly symmetrical motion indicates that the y-direction velocity along the centerline of the flow field is always near zero. This distribution readily brings to mind the scenario of an airfoil vibrating against a fixed wall. Dai *et al.*[39] and Liang *et al.*[40,41] have investigated the mechanical properties of flexible and rigid airfoils vibrating near a wall. Among these studies, flapping wings often achieve higher cruising speeds under the influence of the wall and for the flow and vortex induced by flapping are compressed by the wall, thereby significantly enhancing the rearward propulsion component while increasing the input energy. The behavior of foils near the wall indirectly corroborates the enhancement of propulsion associated with the foil-pair oscillating in out-of-phase motion.

Finally, we discuss the locomotion of the foil pair with phase difference $\varphi = 90°$. As shown in subplots (a)–(d) in Fig. 8, the flow field loses symmetry, and the upper foil 2 has a stronger vortex than foil 1. Subplots (e)–(h) describe the foil pair's pressure distribution. Due to the phase difference, the pressure change is different from the two cases mentioned above. At $t = 0$, the upper foil having swung to the highest point and stopped, the fast-rotating lower foil is the main

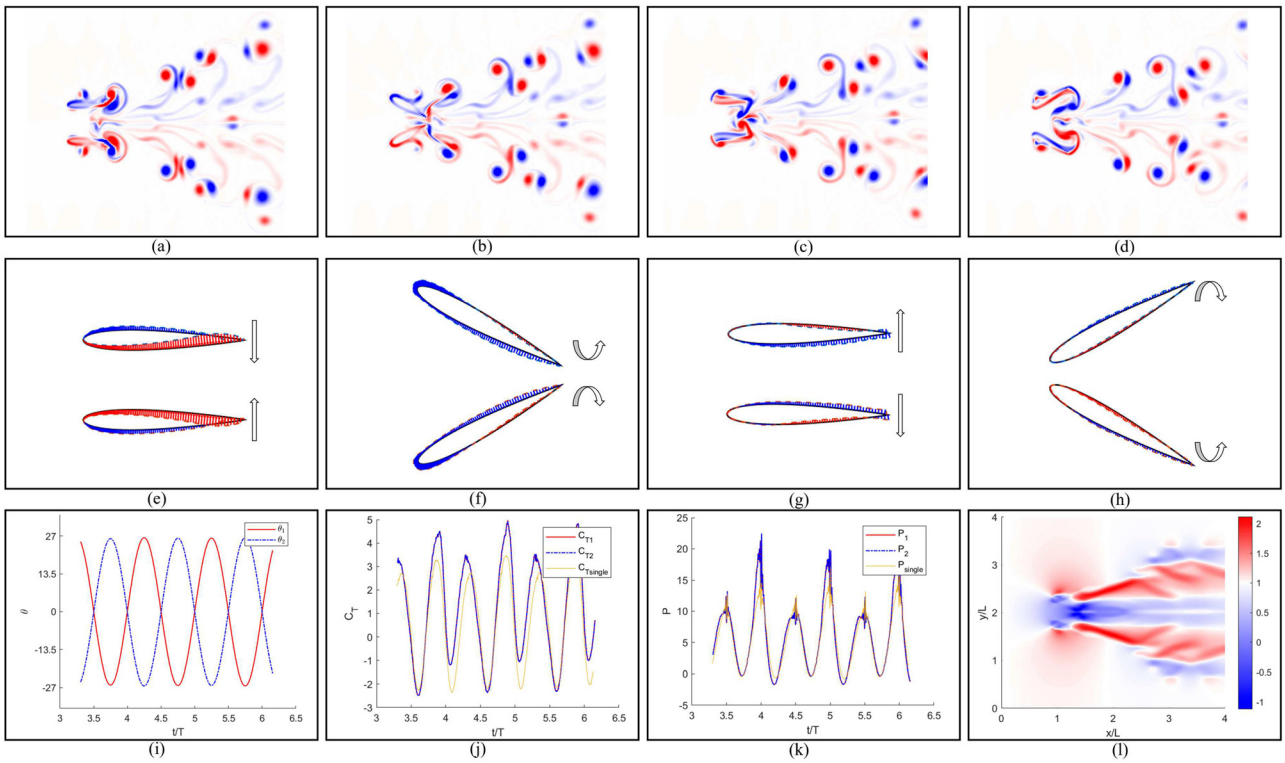

FIG. 7. The multi-physics field analysis of the foil pair when $\varphi = 180^\circ$, and the other parameters are set as $\theta_M = 27^\circ$, $St = 1$, $\hat{d} = 1$. (a)–(d) Vorticity field at $t = 0$, $1/4T, 1/2T, 3/4T$ during a complete motion period. (e)–(h) Pressure distribution on the surface of the foil pair at the corresponding time. (i)–(l) Analysis of flow field data over multiple cycles, where (i) shows the phase of the two foils over three cycles, (j) and (k) shows the change of C_T and energy consumption P over time, and (l) shows the average of the velocity field in the x-direction over three complete cycles. The result of the $\varphi = 180^\circ$ case presents the optimal fluid performance in terms of both thrust and efficiency.

driving structure of the flow field. The vortex generation is similar to the single foil swing as the foil 2 tilt upward. At $t = T/4$, the foil 2 returns to equilibrium, while the lower foil 1 is at its highest point. The two foils are close to each other, and the intensity of vortex generation is also significant, resulting in an asymmetry flow field and a high propulsion efficiency. In the second half of the period from $t = T/2$ to $t = T$, the foils move outwardly and keep a relatively large distance from each other, so the interaction effect is not apparent.

The $\varphi = 90^\circ$ mode also has a distinctive impact on the overall performance of the foil pair. Subplot (j) shows that the foil pair's thrust peak differs for each half period. For the upper foil 2, it is about to start swinging down at $t = 0$ from θ_M to $-\theta_M$ till $t = T/2$, while the lower foil 1 is swinging up at the maximum speed, forming a flow field similar to the case of phase difference $\varphi = 180^\circ$. In the second half period, from $t = T/2$ to $t = T$, foil 2 swings back from $-\theta_M$ to θ_M, while foil 1 swings in the remote lower half area. Therefore, the generated thrust is weaker than in the former half period. However, for the lower foil 1, during its upstroke (specifically from the current $3T/4$ to the next $T/4$), the foil 2 is in the remote upper half area, unable to form an effective jet mode, while consuming more energy. Around $t = T/4$, foil 2 swings down and takes advantage of the tail flow generated by the foil 1, resulting in higher efficiency. The velocity field in subplot (l) also implies the overall efficiency distribution. The average velocity of the upper tail flow is higher than that of the lower tail flow, showing that foil 2 generates a greater thrust in the overall flapping period. Considering that the side-by-side foil pairs have the same motion parameters except for the phase difference, it is remarkable that the lagging foil sacrifices for the leading foil.

IV. CONCLUSION

This study proposes an optimization approach based on the Gaussian process regression algorithm and a fast, robust BDIM fluid mechanics algorithm to optimize and globally predict hydrodynamic performance of a side-by-side flapping foil pair. Through about 10^3 iterations of experiments, we obtain the prediction of 20^4 parameter combinations, and the results agree with those from numerical simulations. The flow field characteristics and propulsion performance of different parameter combinations are compared by controlling four variables ($\hat{d}, \theta_M, \varphi, St$), and it is found that there exist complex coupling relationships among the flapping amplitude, frequency, and phase difference. The distance decrease in the foil pair actually enhances the hydrodynamic interaction. In addition, it is found that the phase difference of the foil pair significantly affects the propulsion efficiency compared with the single flapping foil. In general, the overall propulsion efficiency increases continuously with the phase difference from 0° to 180°. Interestingly, in addition to the

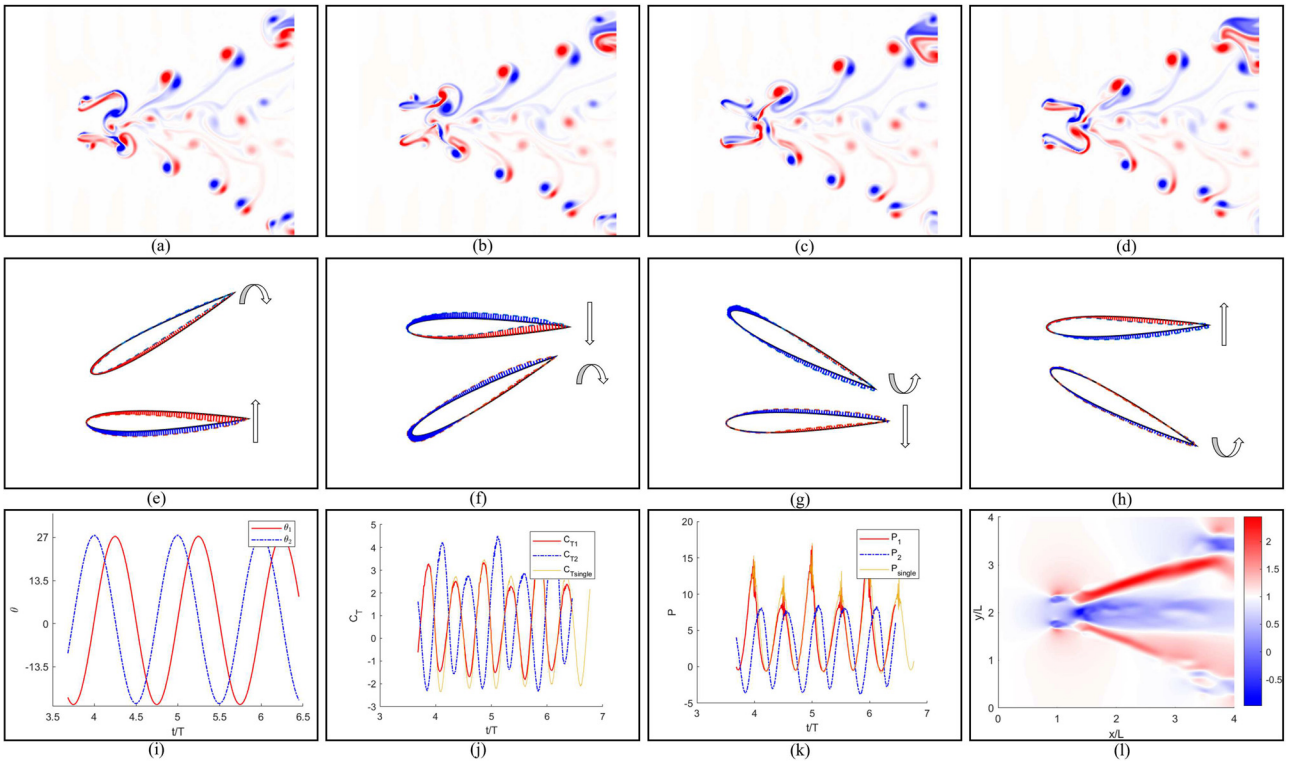

FIG. 8. The multi-physics field analysis of the foil pair when $\varphi = 90^\circ$, and the other parameters are set as $\theta_M = 27^\circ$, $St = 1$, and $\hat{d} = 1$. (a)–(d) Vorticity field at $t = 0$, $T/4$, $T/2$, $3T/4$ during a complete motion period. (e)–(h) Pressure distribution on the surface of the foil pair at the corresponding time. (i)–(l) Analysis of flow field data over multiple cycles, where (i) shows the phase of the two foils over three cycles, (j) and (k) shows the change of C_T and energy consumption P over time, and (l) shows the average of the velocity field in the x-direction over three complete cycles. The result of the $\varphi = 90^\circ$ case shows asymmetry in different aspects.

symmetrical locomotion at in-phase and anti-phase (specifically, the flow fields are symmetrical in time at $t = 0$ and $t = T/2$ for $\varphi = 0^\circ$, and are symmetrical in space for $\varphi = 180^\circ$), when the phase difference is close to 90°, the foil with phase lead will obtain greater efficiency. Meanwhile, the efficiency of the phase-lagged foil is significantly lower than the overall efficiency, even lower than the corresponding value of the single foil with the same locomotion parameters. For this competition mode, a detailed hydrodynamic analysis is conducted to further explore reasons for efficiency differences caused by the phase difference.

The foils in this study are placed in a parallel configuration. Even under such simplified conditions, complex effects between essential parameters and their coupling impacts can still be observed. Given that the rapid parameter-space prediction method is accomplished through a relatively small dataset, it is believed that the application of GPR has great potential in higher-dimensional parameter spaces. Meanwhile, competitive or sacrificial motion patterns also widely exist in the actual operation of fish or bionic underwater vehicles. By altering the phase difference and adopting more complex posture settings, we may better understand the mechanism of fish schooling.

ACKNOWLEDGMENTS

The authors acknowledge the support of the National Key Research and Development Program of China (Grant No. 2022YFC2805200), the National Natural Science Foundation of China (Grant No. 12102365), the Human Frontier Science Program (Grant No. RGY0059/2022), and the Startup funding of New-joined PI of Westlake University with Grant No. 041030150118.

AUTHOR DECLARATIONS

Conflict of Interest

The authors have no conflicts to disclose.

Author Contributions

Boai Sun: Conceptualization (equal); Formal analysis (equal); Methodology (equal); Software (equal); Validation (equal); Visualization (equal); Writing – original draft (equal). **Ruipeng Li:** Supervision (equal); Writing – review & editing (equal). **Weicheng Cui:** Funding acquisition (equal); Supervision (equal). **Dixia Fan:** Conceptualization (equal); Methodology (equal); Resources (equal); Supervision (equal); Writing – review & editing (equal). **Yihan Shen:** Writing – review & editing (equal).

DATA AVAILABILITY

The data that support the findings of this study are available from the corresponding authors upon reasonable request.

APPENDIX A: VALIDATION OF THE BDIM ALGORITHM

To validate the accuracy of BDIM and assess the grid convergence, a comparative study based on the work of Deng *et al.*[42] is conducted. We configured cases with parameters identical to those presented in the previous study, which involved a NACA0015 foil in a flow field at Re = 12 000. The foil rotates about its center of mass located at 0.25 chord length from the leading edge, with a maximum rotation angle of 2°. Different reduced frequencies k varying from 0 to 8 were selected. (It is noting that the k defined by Deng *et al.* satisfies the relationship $k = St * \pi$ as used in this study.) We considered three grid resolutions: 16 (meaning 16 grid points within one chord length), 32, and 64, to calculate the steady-state average thrust coefficient C_T, as shown in Fig. 9.

The results indicate that the BDIM algorithm exhibits a good convergence, and it closely matches the reference literature for small k. However, for k values greater than 6, low-resolution simulations begin to deviate significantly from the reference results. This outcome is expected, as higher-frequency flapping requires finer grid resolution to accurately capture the flow near the rapidly moving tail. It is worth noting that the frequency range of interest in this study corresponds to $St = (0.3, 1.2)$, with reduced frequencies k all below 4. Within this range, the results obtained with a resolution of 32 show minimal differences from those with a higher resolution of 64. Given the high computational demands of this study, the resolution of 32 is adopted in our large-scale simulations to meet the stringent computational speed requirements.

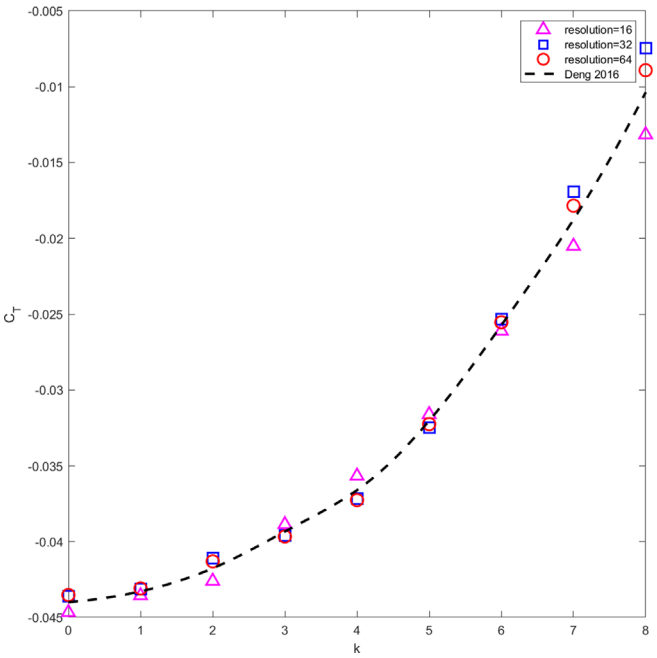

FIG. 9. The validation of the BDIM algorithm.

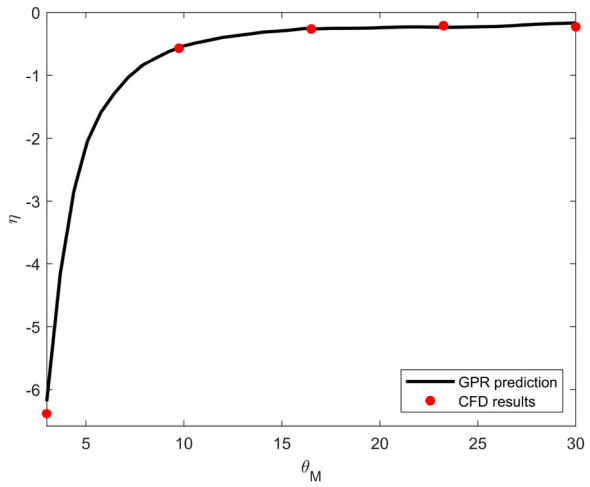

FIG. 10. η of foil flapping under increasing θ_M. Other parameters are set as follows: $\varphi = 45°$, $St = 0.5$, and $\hat{d} = 0.9525$. The black line refers to the GPR prediction, and the red dots are the CFD results.

APPENDIX B: COMPARISONS BETWEEN CFD RESULTS AND GPR PREDICTION

The focus of this paper is on the global prediction of multi-parameter coupling effects. To validate the accuracy of propulsion performance predictions for all four parameters, we selected all four variables and compared the actual CFD results and predictions from the GPR model. Taking the efficiency η as an example, Figs. 10–13 show the comparative results for the four variables, with the GPR predictions represented by solid lines and the CFD results displayed as circles. It can be observed that not only the prediction shows a decent performance compared with the CFD results, but the trends of the efficiency also align well with the predicted values as each parameter varies. It is worth noting that the GPR algorithm

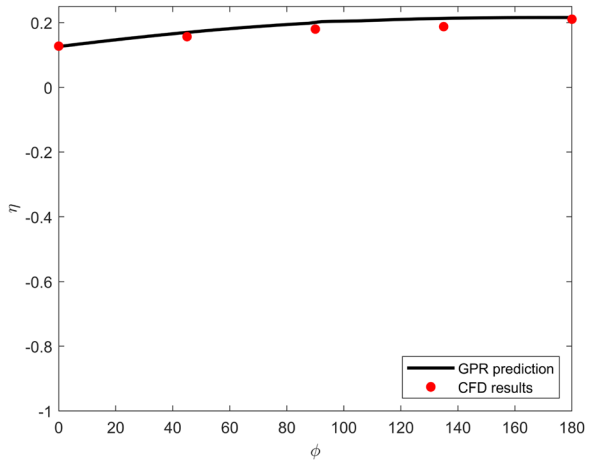

FIG. 11. η of foil flapping under increasing φ. Other parameters are set as follows: $\theta_M = 23°$, $St = 0.90$, and $\hat{d} = 1.135$. The black line refers to the GPR prediction, and the red dots are the CFD results.

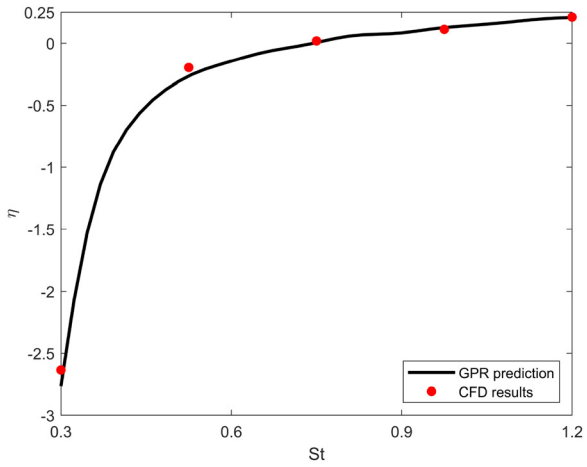

FIG. 12. η of foil flapping under increasing *St*. Other parameters are set as follows: $\theta_M = 16^\circ$, $\varphi = 90^\circ$, and $\hat{d} = 1.135$. The black line refers to the GPR prediction, and the red dots are the CFD results.

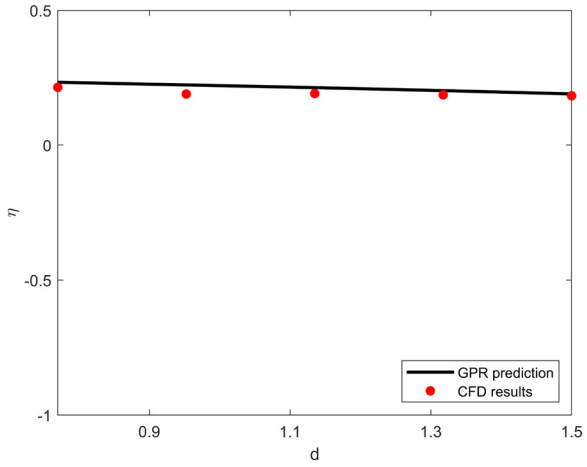

FIG. 13. η of foil flapping under increasing $\hat{d}$. Other parameters are set as follows: $\theta_M = 23^\circ$, $\varphi = 135^\circ$, and $St = 0.9$. The black line refers to the GPR prediction, and the red dots are the CFD results.

tends to provide more accurate predictions near the boundaries of the parameter space, which is related to the iterative nature of the algorithm's kernel functions and may be subject to optimization in future work.

REFERENCES

[1]D. Weihs, "Hydromechanics of fish schooling," Nature **241**, 290–291 (1973).
[2]D. Weihs, "Some hydrodynamical aspects of fish schooling," in *Swimming and Flying in Nature*, edited by T. Y.-T. Wu, C. J. Brokaw, and C. Brennen (Springer US, Boston, MA, 1975), Vol. 2, pp. 703–718.
[3]H.-S. Niwa, "Self-organizing dynamic model of fish schooling," J. Theor. Biol. **171**, 123–136 (1994).
[4]A. J. Ward, J. E. Herbert-Read, D. J. Sumpter, and J. Krause, "Fast and accurate decisions through collective vigilance in fish shoals," Proc. Natl. Acad. Sci. U. S. A. **108**, 2312–2315 (2011).
[5]J. E. Herbert-Read, A. Perna, R. P. Mann, T. M. Schaerf, D. J. Sumpter, and A. J. Ward, "Inferring the rules of interaction of shoaling fish," Proc. Natl. Acad. Sci. U. S. A. **108**, 18726–18731 (2011).
[6]J. E. Herbert-Read, E. Rosén, A. Szorkovszky, C. C. Ioannou, B. Rogell, A. Perna, I. W. Ramnarine, A. Kotrschal, N. Kolm, J. Krause *et al.*, "How predation shapes the social interaction rules of shoaling fish," Proc. R. Soc. B **284**, 20171126 (2017).
[7]B. L. Partridge, "The structure and function of fish schools," Sci. Am. **246**, 114–123 (1982).
[8]C. K. Hemelrijk, D. Reid, H. Hildenbrandt, and J. Padding, "The increased efficiency of fish swimming in a school," Fish Fisheries **16**, 511–521 (2015).
[9]Y. Pan and H. Dong, "Computational analysis of hydrodynamic interactions in a high-density fish school," Phys. Fluids **32**, 121901 (2020).
[10]X. Li, J. Gu, Z. Su, and Z. Yao, "Hydrodynamic analysis of fish schools arranged in the vertical plane," Phys. Fluids **33**, 121905 (2021).
[11]C. Breder, "Vortices and fish schools," Zoologica **50**, 97–114 (1965).
[12]E. Burgerhout, C. Tudorache, S. A. Brittijn, A. P. Palstra, R. P. Dirks, and G. E. van den Thillart, "Schooling reduces energy consumption in swimming male European eels, *Anguilla Anguilla* L.," J. Exp. Marine Biol. Ecol. **448**, 66–71 (2013).
[13]I. Ashraf, H. Bradshaw, T.-T. Ha, J. Halloy, R. Godoy-Diana, and B. Thiria, "Simple phalanx pattern leads to energy saving in cohesive fish schooling," Proc. Natl. Acad. Sci. U. S. A. **114**, 9599–9604 (2017).
[14]Y.-S. Ryuh, G.-H. Yang, J. Liu, and H. Hu, "A school of robotic fish for mariculture monitoring in the sea coast," J. Bionic Eng. **12**, 37–46 (2015).
[15]Z. Zhang, T. Yang, T. Zhang, F. Zhou, N. Cen, T. Li, and G. Xie, "Global vision-based formation control of soft robotic fish swarm," Soft Rob. **8**, 310–318 (2021).
[16]J. W. Newbolt, J. Zhang, and L. Ristroph, "Lateral flow interactions enhance speed and stabilize formations of flapping swimmers," Phys. Rev. Fluids **7**, L061101 (2022).
[17]W. Xu, G. Xu, M. Li, and C. Yang, "Bio-inspired wake tracking and phase matching of two diagonal flapping swimmers," Phys. Fluids **35**, 031902 (2023).
[18]R. Godoy-Diana, J. Vacher, V. Raspa, and B. Thiria, "On the fluid dynamical effects of synchronization in side-by-side swimmers," Biomimetics **4**, 77 (2019).
[19]B. M. Boschitsch, P. A. Dewey, and A. J. Smits, "Propulsive performance of unsteady tandem hydrofoils in an in-line configuration," Phys. Fluids **26**, 051901 (2014).
[20]A. D. Becker, H. Masoud, J. W. Newbolt, M. Shelley, and L. Ristroph, "Hydrodynamic schooling of flapping swimmers," Nat. Commun. **6**, 8514 (2015).
[21]P. A. Dewey, D. B. Quinn, B. M. Boschitsch, and A. J. Smits, "Propulsive performance of unsteady tandem hydrofoils in a side-by-side configuration," Phys. Fluids **26**, 041903 (2014).
[22]F.-B. Tian, W. Wang, J. Wu, and Y. Sui, "Swimming performance and vorticity structures of a mother–calf pair of fish," Comput. Fluids **124**, 1–11 (2016).
[23]G. Xu, W. Duan, and W. Xu, "The propulsion of two flapping foils with tandem configuration and vortex interactions," Phys. Fluids **29**, 097102 (2017).
[24]J. Han, Y. Zhang, and G. Chen, "Effects of individual horizontal distance on the three-dimensional bionic flapping multi-wings in different schooling configurations," Phys. Fluids **31**, 041903 (2019).
[25]L. Dai, G. He, X. Zhang, and X. Zhang, "Intermittent locomotion of a fish-like swimmer driven by passive elastic mechanism," Bioinspiration Biomimetics **13**, 056011 (2018).
[26]G.-J. Dong and X.-Y. Lu, "Characteristics of flow over traveling wavy foils in a side-by-side arrangement," Phys. Fluids **19**, 057107 (2007).
[27]J. Kelly, Y. Pan, A. Menzer, and H. Dong, "Hydrodynamics of body–body interactions in dense synchronous elongated fish schools," Phys. Fluids **35**, 041906 (2023).
[28]J. Ryu, J. Yang, S. G. Park, and H. J. Sung, "Phase-mediated locomotion of two self-propelled flexible plates in a tandem arrangement," Phys. Fluids **32**, 041901 (2020).
[29]D. Dong, W. Chen, and S. Shi, "Coupling motion and energy harvesting of two side-by-side flexible plates in a 3D uniform flow," Appl. Sci. **6**, 141 (2016).
[30]L. Kang, X.-Y. Lu, and W. Cui, "Intermittent swimming of two self-propelled flapping plates in tandem configuration," Phys. Fluids **34**, 011905 (2022).
[31]X. Liu, K. Liu, and H. Huang, "Collective behavior and hydrodynamic advantage of side-by-side self-propelled flapping foils," Phys. Rev. E **105**, 065105 (2022).

[32]A. Gungor, M. S. U. Khalid, and A. Hemmati, "How does switching synchronization of pitching parallel foils from out-of-phase to in-phase change their wake dynamics?," Phys. Fluids **33**, 081901 (2021).
[33]Y. Pan and H. Dong, "Effects of phase difference on hydrodynamic interactions and wake patterns in high-density fish schools," Phys. Fluids **34**, 111902 (2022).
[34]Y. Sun, C. Yan, X. Xiang, H. Zhou, D. Tang, and Y. Zhu, "Towards end-to-end formation control for robotic fish via deep reinforcement learning with non-expert imitation," Ocean Eng. **271**, 113811 (2023).
[35]G. D. Weymouth, D. G. Dommermuth, K. Hendrickson, and D. K.-P. Yue, "Advancements in Cartesian-grid methods for computational ship hydrodynamics," in 26th Symposium on Naval Hydrodynamics, Rome, Italy, 2006.
[36]G. D. Weymouth and D. K. Yue, "Boundary data immersion method for Cartesian-grid simulations of fluid-body interaction problems," J. Comput. Phys. **230**, 6233–6247 (2011).
[37]A. P. Maertens and G. D. Weymouth, "Accurate Cartesian-grid simulations of near-body flows at intermediate Reynolds numbers," Comput. Methods Appl. Mech. Eng. **283**, 106–129 (2015).
[38]C. E. Rasmussen and C. K. Williams, *Gaussian Processes for Machine Learning* (MIT Press Cambridge, MA, 2006).
[39]L. Dai, G. He, and X. Zhang, "Self-propelled swimming of a flexible plunging foil near a solid wall," Bioinspiration Biomimetics **11**, 046005 (2016).
[40]H. Liang, X. Wang, L. Zou, and Z. Zong, "Numerical study of two-dimensional heaving airfoils in ground effect," J. Fluids Struct. **48**, 188–202 (2014).
[41]H. Liang, Z. Zong, and L. Zou, "Nonlinear lifting theory for unsteady wig in proximity to incident water waves. Part 1: Two-dimension," Appl. Ocean Res. **43**, 99–111 (2013).
[42]J. Deng, L. Sun, L. Teng, D. Pan, and X. Shao, "The correlation between wake transition and propulsive efficiency of a flapping foil: A numerical study," Phys. Fluids **28**, 094101 (2016).